Surface plasmon resonance effects of Ti_3C_2 MXene for degradation of antibiotics under full spectrum

Bixin Zhang [a],[1], Yong Wang [a],[1], Zeqiong Wang [a],[1], Guoqiang Tan [a],[*], Tian Liu [a], Shuaijun Feng [a], Yizhe Tan [c], Wenlong Liu [b],[*], Qian Yang [a], Ying Liu [a], Ao Xia [a], Huijun Ren [c], Yuanting Wu [a],[*]

[a] *Shaanxi Key Laboratory of Green Preparation and Functionalization for Inorganic Materials, School of Material Science and Engineering, Shaanxi University of Science & Technology, Xi'an 710021, China*
[b] *School of Electronic Information and Artificial Intelligence, Shaanxi University of Science & Technology, Xi'an 710021, China*
[c] *School of Arts and Sciences, Shaanxi University of Science & Technology, Xi'an 710021, China*

ARTICLE INFO

ABSTRACT

The ML-$(Ti_{1-X}^{2+}Ti_X^{3+})_3C_2V_{Al}^X$ (ML-Ti_3C_2) crystal was exfoliated into the crystal Ti_3C_2 MXene with coexistence of $(Ti_{1-X}^{2+}Ti_X^{3+})_3C_2V_{Al}^X$ MXene and $Ti_2CV_{Al}^X$ MXene by HF etching Ti_3AlC_2 and ultrasonic crushing in water. Ti_3C_2 MXene exhibits the surface plasmon effects of transverse and longitudinal surface plasmon resonance due to its surface holes and internal bound electrons. When excited by the simulated sunlight, the high energy hot holes on the surface of plasma Ti_3C_2 MXene crystal directly oxidize the antibiotics and the organic pollutants. The electrons bound in the crystal lag behind the excitation of holes and migrate to the surface to further degradation. After 150 min of near infrared light irradiation, the degradation rates of tetracycline (TC) and ciprofloxacin (CIP) by Ti_3C_2 MXene are 78.91% and 99.26%, respectively. They are 1.35/1.00 and 1.53/3.11 times of ML-Ti_3C_2 and (001)TiO_2/Ti_3C_2. This study indicates that Ti_3C_2 MXene has significant degradation effects on antibiotics in the full spectral range. Our work intends to provide a valuable reference for the design of the MXene full spectral photocatalyst.

1. Introduction

Graphene was isolated from graphite by Professor Novoselov using a mechanical exfoliation method [1]. It has been reported that graphene has the surface plasmon properties of transverse electric (TE) wave and transverse magnetic (TM) wave. When the imaginary part of graphene conductivity is less than zero, graphene exhibits the TE waves propagating along the surface of graphene and also exhibits semiconductor properties. When the chemical potential of graphene is very large, the in-band transition of its electrons is the main component, and the imaginary part of graphene conductivity is greater than zero, graphene demonstrates TE wave and TM wave perpendicular to the surface of graphene. Graphene possesses metal-like properties and has the LSPR effects of TE and TM [2,3]. In other words, when graphene is doped with other elements, the imaginary part of the conductivity of the doped graphene is greater than zero and the doped graphene reveals TE and TM waves.

MXenes are synthesized by ~~the~~ selectively etching certain atom layers from their precursor MAX phase in HF or a mixture of strong acids and fluoride salts [4]. The general structural formula of MXenes is $M_{n+1}X_nT_x$, where M represents early transition metal elements (such as Ti, V, and Nb), X represents C or N elements, and T_x represents the surface functional groups (such as -O, -OH, and -F) [5,6]. Ti_3C_2 is a graphene-like structural material in MXenes widely represented and studied [7]. Tang Qing et al. concluded that the bare Ti_3C_2 was a magnetic three adjacent C atoms producing the most structurally stable $Ti_3C_2F_2$ and $Ti_3C_2(OH)_2$, making Ti_3C_2 a semiconductor with a very small band gap, that is to say, Ti_3C_2 shows metallic properties, and the F and OH groups are located above the hollow center among the Ti [8,9]. Ti_3C_2 is equivalent to graphene C doped with Ti element. Based on the above research work and theoretical calculation, therefore, Ti_3C_2 MXene should also have TE and TM surface plasmon characteristics. When the photon vibration frequency of incident light is consistent with the natural vibration frequency of Ti_3C_2 MXene, Localized Surface Plasmon

---

* Corresponding authors.
E-mail addresses: tan3114@163.com (G. Tan), lwl1020@126.com (W. Liu), wuyuanting@sust.edu.cn (Y. Wu).
[1] These authors contributed equally to this work.

Resonance (LSPR) is localized on the surface [10]. Thus, local electromagnetic fields are generated on its surface, and this resonant light excitation can produce high energy hot charge carriers and chemical reactions.

In the current application of Ti_3C_2 MXene in the field of photocatalysis, researchers believe that the rich functional groups and the unique layered structure produced by the wet chemical process of preparing Ti_3C_2 MXene make Ti_3C_2 a good adsorbent for heavy metals and organic pollutants, but Ti_3C_2 does not have the photoexcitation ability similar to that of semiconductors, and cannot be used purely as a photocatalytic material. Mashtalir et al. found that Ti_3C_2 had a good adsorption effect on methylene blue aqueous solution under ultraviolet (UV) light irradiation [11].

The construction of heterojunctions by compounding Ti_3C_2 with the semiconductor materials is an effective way to enhance the photocatalytic materials [12–14]. Gao Yupeng et al. prepared TiO_2/Ti_3C_2 composite by hydrothermal method using $TiSO_4$ and Ti_3C_2 as precursors and found that the degradation rate of TiO_2/Ti_3C_2 composites to methyl orange (MO 20 mg/L) reached 98% within 30 min under UV light irradiation, while the degradation rate of Ti_3C_2 was only 42% [15]. Miao Zhiming et al. synthesized an oxygen vacancy modified $TiO_2(TiO_{2-x})/Ti_3C_2$ photocatalyst and found that Ti_3C_2 had almost no degradation effect on bisphenol A, but only having adsorption, and the $(TiO_{2-x})/Ti_3C_2$ photocatalyst reached 67.7% for the same duration [16]. Li Zizhen et al. combined MXene (Ti_3C_2) with a photoactive material (BiOBr) and the system of Ti_3C_2/BiOBr composite achieved 100% complete removal of rhodamine B (RhB) within 30 min, while Ti_3C_2 only removed 26% in 75 min [17].

However, these studies did not take advantage of Ti_3C_2 MXene's surface plasmon properties to degrade antibiotics and organic dyes in the full spectral range. Ti_3C_2 MXene was used as a composite photocatalyst carrier by combining with semiconductor materials, promoting the separation of photocarriers, limiting the size of photocatalyst and enhancing the adsorption of reactants, which could improve the activities of the degrading pollutants, Jing Wang et al. found that the MXene material had an excellent photothermal conversion performance thanks to strong light absorption and the LSPR effect, that is, it could effectively collect solar energy, and store and utilize the transformed heat energy [18,19]. Therefore, the materials with the LSPR effect could promote the transfer of hot electrons and charge separation, thus enhancing its photocatalytic performance [20–23]. However, the relative stability of antibiotics, the difficulty of natural degradation, and the serious harm to organisms (health threat and bacterial resistance) have become a research focus, and the removal of antibiotics is still a big challenge [24–27].

In this work, ML-Ti_3C_2 obtained by HF etching Ti_3AlC_2 was further prepared by ultrasonic crushing in water, and the surface plasmon effect of the few layer Ti_3C_2 MXene was verified. The electron cloud distribution on the surface of the few-layer Ti_3C_2 MXene and the decomposition process of photoexcited degradation of antibiotics and organic dyes were studied by density functional theory (DFT) calculation and the liquid chromatography mass spectrometer (LC-MS) test. The degradation effects of MXene on antibiotics and organic dyes in the full spectral range were analyzed. The photocatalytic mechanism of the few layer Ti_3C_2 MXene on antibiotics and organic dyes in the full spectral range was also analyzed. Our work provides reference for the application of Ti_3C_2 MXene in photocatalysis.

2. Experimental section

2.1. Preparation of Ti_3C_2 MXene

10 g of Ti_3AlC_2 precursor was weighed and slowly added into 100 ML HF to obtain 0.1 g/ML reaction solution, which was stirred at room temperature for 27 h for the ensuing acid corrosion reaction. After the reaction, the suspension was washed with a large amount of

deionized water for several times until the pH of the supernatant was greater than 6.5, and then washed with ethanol for three times. The multilayer Ti_3C_2 (ML-Ti_3C_2) powder was obtained by vacuum drying at 60 °C for 12 h. 1 g ML-Ti_3C_2 powder was dispersed in 30 ML deionized water to obtain 25 mg/L ML-Ti_3C_2 solution, and then ultrasonically crushed for 1 h (70 W). Finally, Ti_3C_2 MXene was collected by high speed centrifugation. In addition, 200 mg of Ti_3C_2 MXene was weighed and added to 30 ML of HCl (1.0 mol/L) and 0.33 g of $NaBF_4$ was added as a crystal surface control agent. The mixed solution was dispersed evenly by stirring with ultrasound, and subsequently transferred to a polytetrafluoroethylene hydrothermal reactor and reacted hydrothermally at 160 °C for 12 h. After cooling to room temperature, the sample was washed and dried to finally collect the exposed (001) crystal planes of TiO_2/Ti_3C_2 composite. The prepared sample of (001)TiO_2/Ti_3C_2-200 was used as the contrast sample.

2.2. Characterization of Ti_3C_2 MXene

The phase composition and the crystal structure of the samples were characterized by an X-ray diffraction (XRD, D/max-2200 PC, Rigaku, Cu Kα, λ = 0.15406 nm, 40 kV, 40 mA) at a scanning rate of 7° min^{-1}. The internal valence bond structures of the samples were characterized by a Raman spectroscopy (Raman, DXRxi, THEM America, excitation wavelength: 532 nm). The molecular structures of the samples were characterized by a Fourier infrared spectrometer (FT-IR, Vertex70), and potassium bromide was used as the test background. The surface morphology of the samples was characterized by a Field emission scanning electron microscope (FE-SEM, SU8100, 15 kV). The microstructures of the samples were characterized by a transmission electron microscopy (TEM, FEI-Tecnai G2 F20). The light absorption characteristics of the samples were reflected by a UV–vis-NIR diffuse reflectance spectrum (DRS, Cray 5000, Agilent, U.S.A.), and the test range was 200–2200 nm. The element composition and chemical bonds of the samples were characterized by an X-ray photoelectron spectroscopy (XPS, XSAM800). Thermo Avantage 4.5 software was used to fit the test result, and C 1 s at 284.6 eV was used as the standard C for calibration. The mineralization ability of the samples was characterized by a high-performance liquid chromatography (HPLC, watersE2695). Possible intermediates and degradation pathways of TC were analyzed by an Ultimate 3000 UHPLC-Q Exactive liquid chromatography/mass spectrometer. The photocurrent curves (i-t) and an AC electrical impedance spectroscopy (EIS) of the samples were measured by CHI660E electrochemical workstation. A three-electrode system was adopted, with the film electrode as a working electrode, the Pt electrode as a counter-electrode, and the Ag/AgCl electrode as a reference electrode, and the concentration of 0.1 mol/L Na_2SO_4 solution was used as the electrolyte. The possible intermediate products and the degradation pathways of TC were analyzed by the LC-MS technology, and the LC-MS was recorded on an Ultimate 3000 UHPLC-Q Exactive liquid chromatography/mass spectrometer (Thermo Scientific, US). The interfacial charge distribution and the differential charge density of the samples were obtained by DFT simulation, and the structure model was used to restore the real structure of the materials obtained by the experiment to the maximum extent. The electromagnetic field intensity around the sample was simulated by the finite difference time domain (FDTD) calculation, and the excitation wavelength was set at 960 nm and 580 nm. The FDTD method simulates the electric field distribution by emitting electrical pulses at the boundary. The average electric field enhancement factor was obtained by calculating the average electric field intensity enhancement within the grid.

2.3. Photocatalysis experiment of Ti_3C_2 MXene

The photocatalytic activity of the samples was evaluated by degrading 10 mg/L tetracycline hydrochloride (TC), 10 mg/L ciprofloxacin (CIP), 5 mg/L rhodamine B (RhB) and 5 mg/L methyl orange

(MO). The photocatalytic degradation experiment was carried out on an XPA-7 photoreactor, and different types of lamps and filters were used to simulate the specific light sources. A 500 W xenon lamp was selected to simulate sun light (200–2500 nm), a 300 W mercury lamp to simulate UV light (200–420 nm), a 500 W xenon lamp and a 420 nm cut-off filter to simulate visible light (420–780 nm), and a 500 W xenon lamp and a transparent filter light of 780 nm were selected to simulate near infrared (NIR) light (780–2500 nm). The absorbance of degradation results was measured by an SP-756 P UV–visible spectrophotometer. The specific operation was as follows: 50 mg of the sample was weighed into a quartz test tube, and then 50 ML of the degradation liquid was added. The adsorptions-desorption balance was reached after the dark reaction of 30 min. About 5 ML suspension was taken out every 30 min during the illumination stage. After centrifugation, the supernatant was taken for testing and analyzing according to the data changes of maximum absorption wavelength. In the photocatalytic degradation process, the active species were detected by adding p-benzoquinone (pBQ/1 mg), ethylenediaminetetraacetic acid disodium salt (EDTA-2Na/1 mmol), and tert-butanol (PBA/1 ML) as the active species trapping agents. In addition, the multi-channel photocatalytic reaction system (PCX50C Discover) was used for monochromatic photodegradation experiments. The wavelengths of monochromatic light were 740 nm (5 W), 850 nm (5 W), 940 nm (5 W) and 1100 nm (5 W), respectively.

3. Results and discussion

3.1. Structure, morphology and optical performance of Ti_3C_2 MXene

The XRD patterns of Ti_3C_2 MXene are shown in Fig. 1(a). After HF etching Ti_3AlC_2 (JCPDS No.52–0875), the strongest (104) crystal plane

diffraction peak of Ti_3AlC_2 at 39.1° almost disappears, and the diffraction peaks of (002) crystal plane at 9.5° and of (004) crystal plane at 19.2° are broadened and shifted to a lower angle shown in Fig. 1(b), which indicates that the Al atomic layer in the Ti_3AlC_2 molecular layer is successfully etched and transformed into two-dimensional ML-Ti_3C_2 [9]. Compared with ML-Ti_3C_2, the diffraction peaks of the (002) plane of Ti_3C_2 MXene are shifted to low angles because after the multilayer ML-Ti_3C_2 is exfoliated to form a few layers of Ti_3C_2 MXene, the interlayer spacing is further enlarged, which is consistent with the literature reports[28,37]. After Ti_3C_2 MXene is treated by hydrothermal oxidation method, $2\theta= 25.2°, 37.0°, 37.8°, 38.6°, 48.1°, 53.9°, 55.1°$ and $62.7°$ correspond to the diffraction peaks of (101), (103), (004), (112), (200), (105), (211) and (204) crystal planes of anatase TiO_2 (JCPDS No.21–1272) respectively. This is because part of Ti_3C_2 MXene is oxidized to TiO_2 [29], and the diffraction peak of Ti_3C_2 MXene is weakened. The Raman spectra of Ti_3C_2 MXene is shown in Fig. 1(c). For ML-Ti_3C_2 and Ti_3C_2 MXene, the four characteristic peaks located at 153 cm^{-1}, 271 cm^{-1}, 404 cm^{-1} and 605 cm^{-1} are attributed to $\omega1$, $\omega2$, $\omega3$ and $\omega4$ Raman active phonon vibration modes, respectively [30]. The $\omega1$, $\omega2$, $\omega3$ and $\omega4$ Raman active phonon vibration modes of Ti_3C_2 MXene are obviously enhanced due to the in-band transition of Ti_3C_2 MXene electrons along the surface vibration perpendicular to Ti_3C_2 MXene, which forms the surface plasmon body wave TM transverse magnetic wave, resulting in the enhanced surface Raman scattering (SERS) of Ti_3C_2 MXene, which suggests that Ti_3C_2 MXene may have TE and TM vibrations similar to graphene [31]. In addition, when ML-Ti_3C_2 is exfoliated into Ti_3C_2 MXene, the thinning makes the TE and TM of Ti_3C_2 MXene enhanced, and the synergistic effects of the enhancement of TE and TM result in the blue-shift of the characteristic peak of $\omega3$. After oxidation treatment, the vibration peak of Ti_3C_2 MXene is
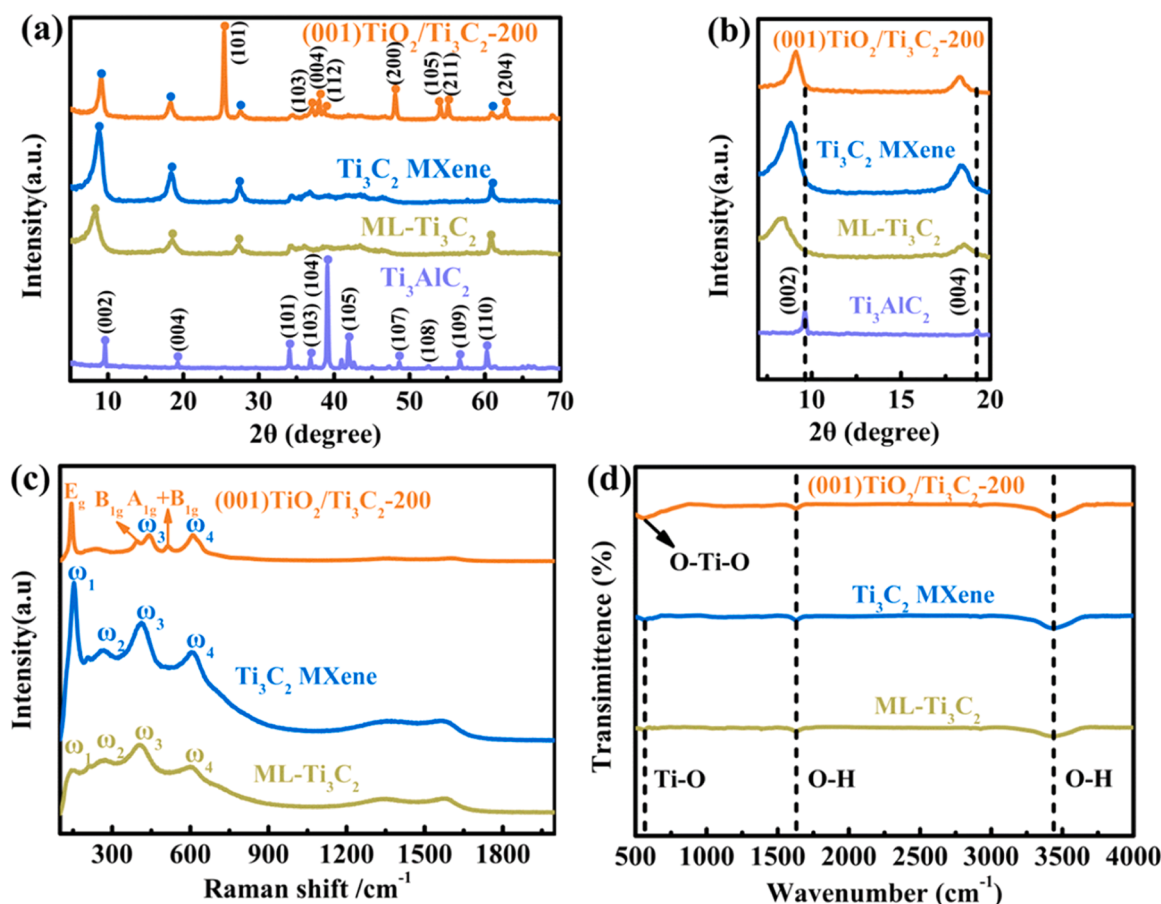

Fig. 1(. a) The XRD patterns of Ti_3C_2 MXene, (b) partially enlarged details of 7–20°, (c) the Raman spectra of Ti_3C_2 MXene, (d) the IR spectra of Ti_3C_2 MXene.

weakened, ω1 and ω2 peaks almost disappear, the blue shift appears in the ω3 characteristic peak, and the peaks at 143 cm^{-1}, 396 cm^{-1} and 514 cm^{-1} belong to Eg, $B_{1\,g}$, and $A_{1\,g}+B_{1\,g}$ modes of the anatase phase TiO_2, respectively [32], indicating that the anatase phase TiO_2 is generated in the hydrothermal oxidation process of Ti_3C_2 MXene. In addition, D and G peaks of carbon in Ti_3C_2 are detected at both 1350 cm^{-1} and 1590 cm^{-1} peaks, while D peak represents the defect of lattice of carbon atom, and G peak represents the in-plane stretching vibration of carbon atom SP^2 hybrid [33], which reveals that the graphene layer is formed on the surface of Ti_3C_2 MXene. The D and G peaks corresponding to (001)TiO_2/Ti_3C_2 obtained by hydrothermal oxidation of Ti_3C_2 MXene are obviously weakened, further indicating that Ti_3C_2 graphene C exists on the surface of MXene [34]. The IR spectroscopy of Ti_3C_2 MXene is shown in Fig. 1(d). The wide peaks at 3435 cm^{-1} and 1630 cm^{-1} are attributed to the O-H stretching vibration peak, which proves that ML-Ti_3C_2, Ti_3C_2 MXene, and (001)TiO_2/Ti_3C_2-200 have -OH adsorption. While ML-Ti_3C_2 and Ti_3C_2 MXene at 596 cm^{-1} are attributed to the Ti-O stretching vibration peak, showing that the Ti_3C_2 surface absorbs -OH to form the Ti-O bond [35].

Fig. 2 shows the SEM and TEM images of Ti_3C_2 MXene. Ti_3AlC_2 is etched by HF to form 25 layers of 5 μm thick accordion-like ML-Ti_3C_2, indicating that Al is removed from Ti_3AlC_2 layers and there is a clear spacing between the layers (Fig. 2(a)). After ultrasonic treatment, about 9 layers of 2.5 μm thick Ti_3C_2 MXene are obtained, and the thickness of Ti_3C_2 MXene is obviously thinner (Fig. 2(b)). TEM image shows the Ti_3C_2 MXene lamellar structure clearly (Fig. 2(c)). HRTEM obviously shows that the adjacent lattice spacings of 0.98 nm and 0.26 nm correspond to the (002) and (101) crystal planes of Ti_3C_2 MXene, respectively (Fig. 2(d)). After oxidation treatment of Ti_3C_2 MXene, TiO_2 nanosheets about 800 nm wide and 200 nm thick are embedded on Ti_3C_2 MXene (Fig. 2(e)). The EDS spectrum shows that the (001)TiO_2/Ti_3C_2-200 sample is composed of Ti, O, and C elements, the contents of Ti, O, and C elements are 55.83%, 32.28% and 11.97%, respectively, and the high oxygen content confirms the formation of TiO_2/Ti_3C_2 composite (Fig. 2(f))[36]. TEM image shows the interface between TiO_2 and Ti_3C_2 MXene clearly, and TiO_2 nanosheets are embedded in the interlayer and the surface of the lamellar Ti_3C_2 (Fig. 2(g)). HRTEM can distinctly show that the adjacent lattice spacings of 0.98 nm and 0.35 nm correspond to the Ti_3C_2 MXene (002) crystal plane and the anatase TiO_2 (101) crystal plane (Fig. 2(h)). The above analyses show that Ti_3AlC_2 is etched by HF to obtain the multilayer ML-Ti_3C_2, and the thin lamellar Ti_3C_2 MXene is prepared by ultrasonically crushing. The TiO_2/Ti_3C_2 MXene photocatalyst with the exposed (001) crystal plane is prepared by hydrothermal oxidation method with TiO_2 nanosheets embedded in the interlayer and the surface of the lamellar Ti_3C_2 MXene.

Fig. 3 shows the XPS spectra of Ti_3C_2 MXene. The binding energy of the samples is calibrated by C 1 s orbital binding energy (284.6 eV). The full spectrum images of ML-Ti_3C_2, Ti_3C_2 MXene, and (001)TiO_2/Ti_3C_2-200 confirm the existence of Ti, C, O and F elements, and F element is derived from the F ion residues of HF and $NaBF_4$ in the synthesis process and adsorbed in the interlayer (Fig. S1) [37]. The Ti 2p orbital of ML-Ti_3C_2 can be fitted into three groups of the double peaks (Fig. 3(a)): Ti $2p_{3/2}$ peak and Ti $2p_{1/2}$ peak. The binding energies of Ti $2p_{3/2}$ peak at 455.77 eV, 457.12 eV and 457.77 eV are attributed to Ti^{2+}, Ti^{3+} and Ti^{4+}, respectively. The binding energies of Ti $2p_{1/2}$ peak at 460.98 eV, 463.09 eV and 465.15 eV are attributed to Ti^{2+}, Ti^{3+} and Ti^{4+}, respectively [34,36]. The fitting results show that Ti^{2+}, Ti^{3+} and Ti^{4+} contents are 83.54%, 8.10% and 8.37%, respectively. The Ti 2p orbital of Ti_3C_2 MXene can also be fitted into three groups of the double peaks: Ti $2p_{3/2}$ peak and Ti $2p_{1/2}$ peak. The binding energies of Ti $2p_{3/2}$ peak at 455.90 eV, 457.29 eV and 458.59 eV are attributed to Ti^{2+}, Ti^{3+} and Ti^{4+}, respectively. The binding energies of Ti $2p_{1/2}$ peak at 461.18 eV, 463.33 eV and 465.03 eV are attributed to Ti^{2+}, Ti^{3+} and Ti^{4+}, respectively. The fitting results show that Ti^{2+}, Ti^{3+} and Ti^{4+} contents are 64.04%, 19.31% and 16.64%, respectively. Ti_3C_2 MXene is prepared by ultrasonically crushing ML-Ti_3C_2, Ti^{2+} content is decreased significantly, and Ti^{3+} content is increased, which indicates that part of Ti^{2+} electron loss is converted to Ti^{3+}. While the increase of Ti^{4+} content is due to the further slow oxidation of Ti^{2+} into Ti^{4+} during ML-Ti_3C_2 ultrasound treatment, which is consistent with literature reports [38]. The Ti 2p orbital of (001)TiO_2/Ti_3C_2-200 can also be fitted into three groups of the double peaks: Ti $2p_{3/2}$ peak and Ti $2p_{1/2}$ peak. The binding energies of Ti $2p_{3/2}$ peak at 455.82 eV, 457.27 eV and 458.98 eV are attributed to Ti^{2+}, Ti^{3+} and Ti^{4+}, respectively. The binding energies of Ti $2p_{1/2}$ peak at 461.59 eV, 463.24 eV and 464.87 eV are attributed to Ti^{2+}, Ti^{3+} and Ti^{4+}, respectively. The fitting results show that Ti^{2+}, Ti^{3+} and Ti^{4+} contents are 26.01%, 32.72% and 52.07%, respectively. After hydrothermal oxidation of Ti_3C_2 MXene, Ti^{2+} content is decreased significantly, while Ti^{4+} content is increased, indicating that part of Ti_3C_2 MXene is oxidized to TiO_2 under hydrothermal conditions (Fig. 3 (a)). The C 1s spectra of ML-Ti_3C_2, Ti_3C_2 MXene and (001)TiO_2/-Ti_3C_2-200 can be fitted to four peaks, located at 281.74 eV, 282.78 eV, 284.54 eV and 286.00 eV, corresponding to Ti-C, C-Ti-O, C-C (graphite carbon) and C-O species, respectively. The C 1s peak at 284.54 eV is
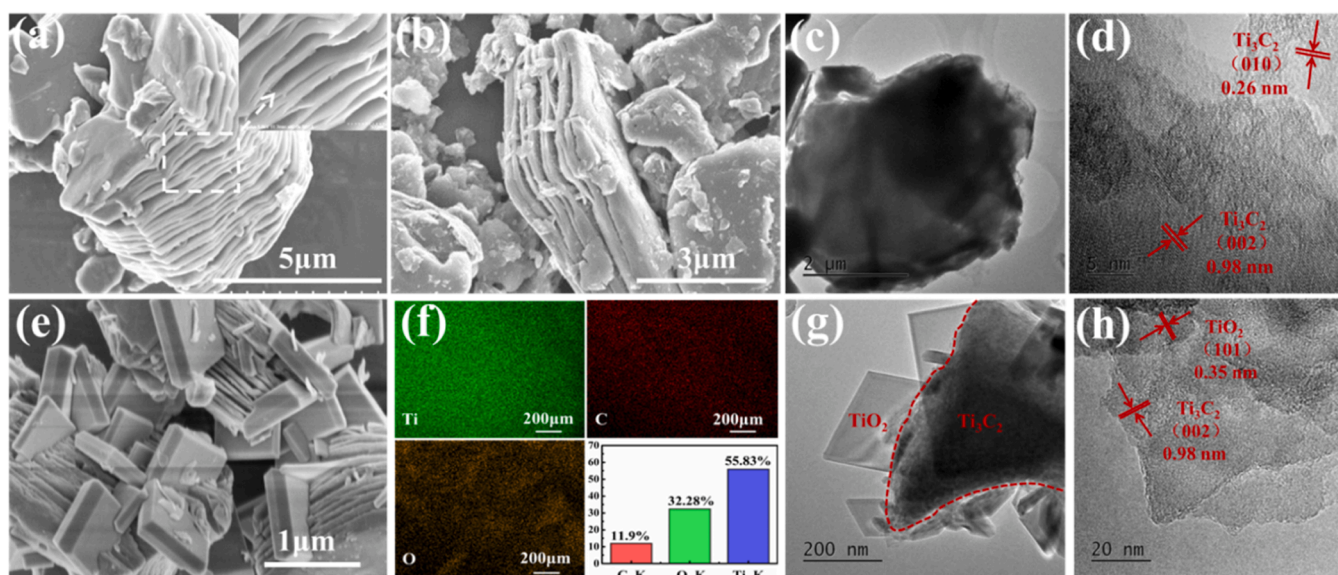

Fig. 2. SEM, TEM and TEM EDX mapping images of the samples (a) ML-Ti_3C_2, (b)-(d) Ti_3C_2 MXene, (e)-(h) (001)TiO_2/Ti_3C_2-200.
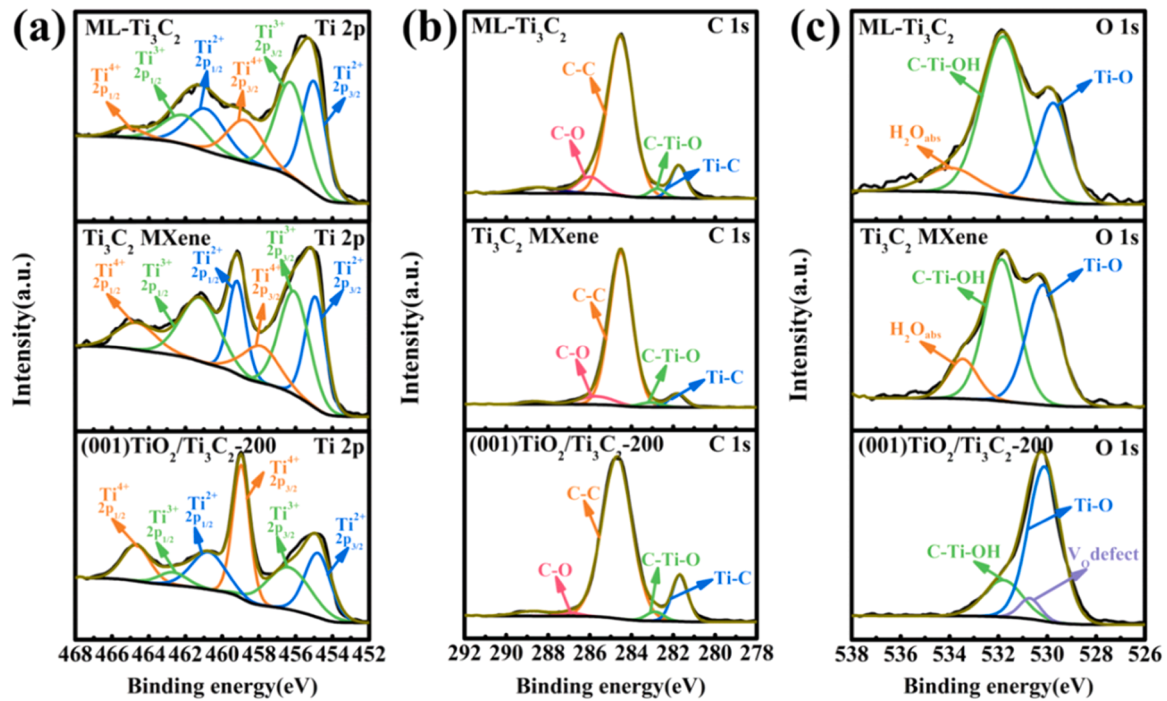
Fig. 3. XPS spectra of (a) Ti 2p, (b) C1 S and (c) O 1 S of Ti_3C_2 MXene.

caused by hydrocarbons adsorbed on the surface of the instrument. Among them, The C-Ti-O bond is formed by the adsorption of -OH on the surface of Ti_3C_2 (Fig. 3(b)) [39]. Ti-C should be the main chemical bond in ML-Ti_3C_2 and Ti_3C_2 MXene. The O1s spectra of ML-Ti_3C_2 and Ti_3C_2 MXene can be fitted into three peaks at 529.76 eV, 531.86 eV and 533.89 eV, respectively, belonging to Ti-O (lattice oxygen), C-Ti-OH and H_2O_{abs}. The O 1 s spectra of (001)TiO_2/Ti_3C_2-200 can be fitted into three peaks at 530.11 eV, 530.71 eV and 531.8 eV, respectively, belonging to Ti-O (lattice oxygen), V_O and C-Ti-OH, with the contents of 72.93%, 6.42% and 20.65%, respectively (Fig. 3(c)). Based on the above analyses, the following results can be obtained: Al atom layer of lattice in the Ti_3AlC_2 crystal is etched by HF and transformed into two-dimensional ML-Ti_3C_2, forming Al vacancy (V_{Al}^X), the electrical neutrality of the whole ML-$(Ti_{1-X}^{2+}Ti_X^{3+})_3C_2V_{Al}^X$ crystal cannot be satisfied, and each Al^{3+} will generate three holes, which are distributed on the surface of the ML-$(Ti_{1-X}^{2+}Ti_X^{3+})_3C_2V_{Al}^X$ crystal, as shown in the reaction Formula 1–1. ML-$(Ti_{1-X}^{2+}Ti_X^{3+})_3C_2V_{Al}^X$ forms a positive center, which binds the excess valence electrons in the ML-$(Ti_{1-X}^{2+}Ti_X^{3+})_3C_2V_{Al}^X$ crystal into its own crystal, and further adsorbs OH- and F- in the solution to form ML-$(Ti_{1-X}^{2+}Ti_X^{3+})_3C_2V_{Al}^X(OH)_2$ and ML-$(Ti_{1-X}^{2+}Ti_X^{3+})_3C_2V_{Al}^XF_2$, as shown in the reaction Formula 1–2. When ultrasonically exfoliated in aqueous solution, the adsorbed OH⁻ and F⁻ are exfoliated by ultrasonic energy. The full spectrum XPS diagram (Fig.S1) also shows that OH⁻ and F⁻ of Ti_3C_2 MXene are decreased, and at the same time, ultrasonic energy can exfoliate ML-$(Ti_{1-X}^{2+}Ti_X^{3+})_3C_2V_{Al}^X$ into $(Ti_{1-X}^{2+}Ti_X^{3+})_3C_2V_{Al}^X$ MXene and $Ti_2CV_{Al}^X$ MXene, which is equivalent to further separate Ti_3C_2 and Ti_2C in the ML-$(Ti_{1-X}^{2+}Ti_X^{3+})_3C_2V_{Al}^X$ cell. The exfoliating exposes more Ti^{3+} in $(Ti_{1-X}^{2+}Ti_X^{3+})_3C_2V_{Al}^X$, which increases Ti^{3+} content but decreases Ti^{2+}. Due to the valence state change of Ti^{2+}/Ti^{3+}, there are electrons in crystal $(Ti_{1-X}^{2+}Ti_X^{3+})_3C_2V_{Al}^X$ MXene, which leads to the distribution of holes on the surface of crystal Ti_3C_2 MXene V_{Al}^X and the formation of a positive center, which can bind the excess valence electrons in the Ti_3C_2 MXeneV_{Al}^X crystal to its own crystal, as shown in the reaction Formula 1–3. $(Ti_{1-X}^{2+}Ti_X^{3+})_3C_2V_{Al}^X$ MXene and $Ti_2CV_{Al}^X$ MXene are oxidized to (001)TiO_2/Ti_3C_2-200, Ti_2C MXeneV_{Al}^X is first oxidized to TiO_2, and part of Ti^{2+} in $(Ti_{1-X}^{2+}Ti_X^{3+})_3C_2V_{Al}^X$ MXene is oxidized to TiO_2, which results in

the increase of Ti^{4+} in (001)TiO_2/Ti_3C_2 and the decrease of Ti^{2+} content. At the same time, more electrons are stored in (001)TiO_2/Ti_3C_2-200, as shown in the reaction Formula 1–4. In addition, oxygen vacancy is formed when Ti_3C_2 MXene is oxidized to TiO_2 due to hypoxia.
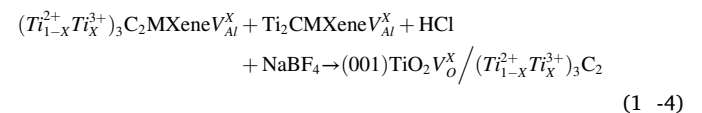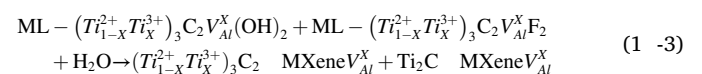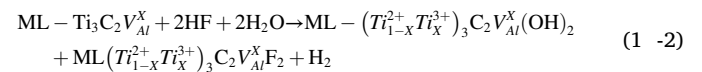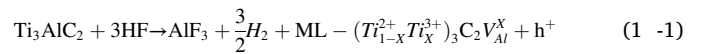
$$Ti_3AlC_2 + 3HF \rightarrow AlF_3 + \frac{3}{2}H_2 + ML - (Ti_{1-X}^{2+}Ti_X^{3+})_3C_2V_{Al}^X + h^+ \quad (1\text{ -}1)$$

$$ML - Ti_3C_2V_{Al}^X + 2HF + 2H_2O \rightarrow ML - (Ti_{1-X}^{2+}Ti_X^{3+})_3C_2V_{Al}^X(OH)_2 \\ + ML(Ti_{1-X}^{2+}Ti_X^{3+})_3C_2V_{Al}^XF_2 + H_2 \quad (1\text{ -}2)$$

$$ML - (Ti_{1-X}^{2+}Ti_X^{3+})_3C_2V_{Al}^X(OH)_2 + ML - (Ti_{1-X}^{2+}Ti_X^{3+})_3C_2V_{Al}^XF_2 \\ + H_2O \rightarrow (Ti_{1-X}^{2+}Ti_X^{3+})_3C_2 \quad MXeneV_{Al}^X + Ti_2C \quad MXeneV_{Al}^X \quad (1\text{ -}3)$$

$$(Ti_{1-X}^{2+}Ti_X^{3+})_3C_2MXeneV_{Al}^X + Ti_2CMXeneV_{Al}^X + HCl \\ + NaBF_4 \rightarrow (001)TiO_2V_O^X / (Ti_{1-X}^{2+}Ti_X^{3+})_3C_2 \\ (1\text{ -}4)$$

Fig. 4(a) shows the EPR spectra of Ti_3C_2 MXene. ML-Ti_3C_2, Ti_3C_2 MXene and (001)TiO_2/Ti_3C_2-200 all show EPR signals when the g value is about 2.003, which is attributed to defects within the range of g= 2.001–2.005 [40], but the ML-Ti_3C_2 signal is weak. Therefore, it can be determined that there are defects in all these three samples, and the defect concentration of (001)TiO_2/Ti_3C_2-200 is slightly higher than that of Ti_3C_2 MXene, which is caused by the formation of oxygen vacancies when part of Ti_3C_2 MXene is oxidized to TiO_2 in the hydrothermal sealing system due to anoxia. There is V_{Al}^X on Ti_3C_2 in (001)TiO_2/Ti_3C_2, and oxygen vacancies exist in TiO_2, resulting in a greater defect concentration than that of Ti_3C_2 Mxene in (001)TiO_2/Ti_3C_2 [25].

Fig. 4(b) shows the UV–vis-NIR DRS diagram of Ti_3C_2 MXene. ML-Ti_3C_2 and Ti_3C_2 MXene have light absorption in the UV–vis-NIR spectral range, and both have two obvious absorption peaks at 580 nm and 960 nm, which are attributed to transverse surface plasmon resonance (TE) and longitudinal surface plasmon resonance (TM) of ML-Ti_3C_2 and Ti_3C_2 MXene, respectively [41,42]. Because Ti_3C_2 MXene has more defects than ML-TI_3C_2, Ti_3C_2 MXene has stronger light absorption in UV–vis-NIR spectrum. In addition, ML-Ti_3C_2 and Ti_3C_2 MXene have an absorption peak at 320 nm in Fig. 4(b), which is attributed to the
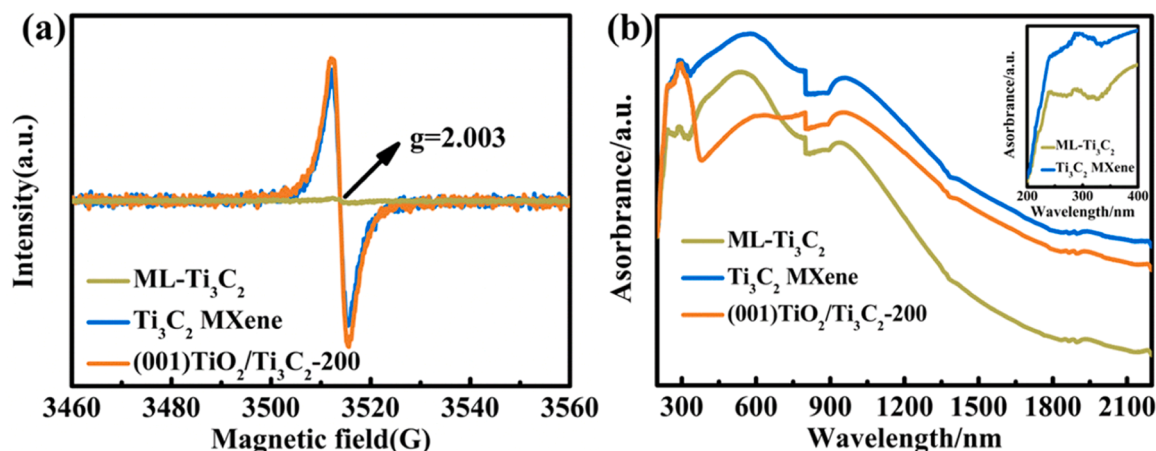
Fig. 4. (a) EPR spectra of Ti_3C_2 MXene, (b) UV–vis-NIR DRS of Ti_3C_2 MXene.

absorption peak of anatase TiO_2. This is caused by Ti_3C_2 oxidation on the surface during acid etching and ultrasonically crushing in water, which is consistent with the XPS analysis results. After the hydrothermal oxidation of Ti_3C_2 MXene, the absorption capacity of (001)TiO_2/Ti_3C_2-200 is decreased significantly in the UV–vis-NIR spectrum range of 400–2100 nm, but is increased at 320 nm, which belongs to the absorption peak of anatase TiO_2. Therefore, the few-layer Ti_3C_2 MXene prepared by ultrasonication of the multilayer ML-Ti_3C_2 forms more defects and has a full spectral response. The structural changes during the formation of Ti_3C_2 MXene are shown in Fig. 5.

3.2. Photocatalytic performance of Ti_3C_2 MXene

Fig. 6 shows the degradation curves and the degradation rates of Ti_3C_2 MXene on TC under different illuminations. After 150 min UV light illumination, the degradation rates of P25, ML-Ti_3C_2, Ti_3C_2 MXene and (001)TiO_2/Ti_3C_2-200 are 95.4%, 72.99%, 54.02% and 67.32%, respectively (Fig. 6(a)), and the degradation rate constants (K) are 0.01531 min^{-1}, 0.00338 min^{-1}, 0.00298 min^{-1} and 0.0046 min^{-1}, respectively (Fig. S2(a)). After 150 min of vis light illumination, the degradation rates of ML-Ti_3C_2, Ti_3C_2 MXene and (001)TiO_2/Ti_3C_2-200 are 52.03%, 77.81% and 38.28%, respectively (Fig. 6(b)), and the
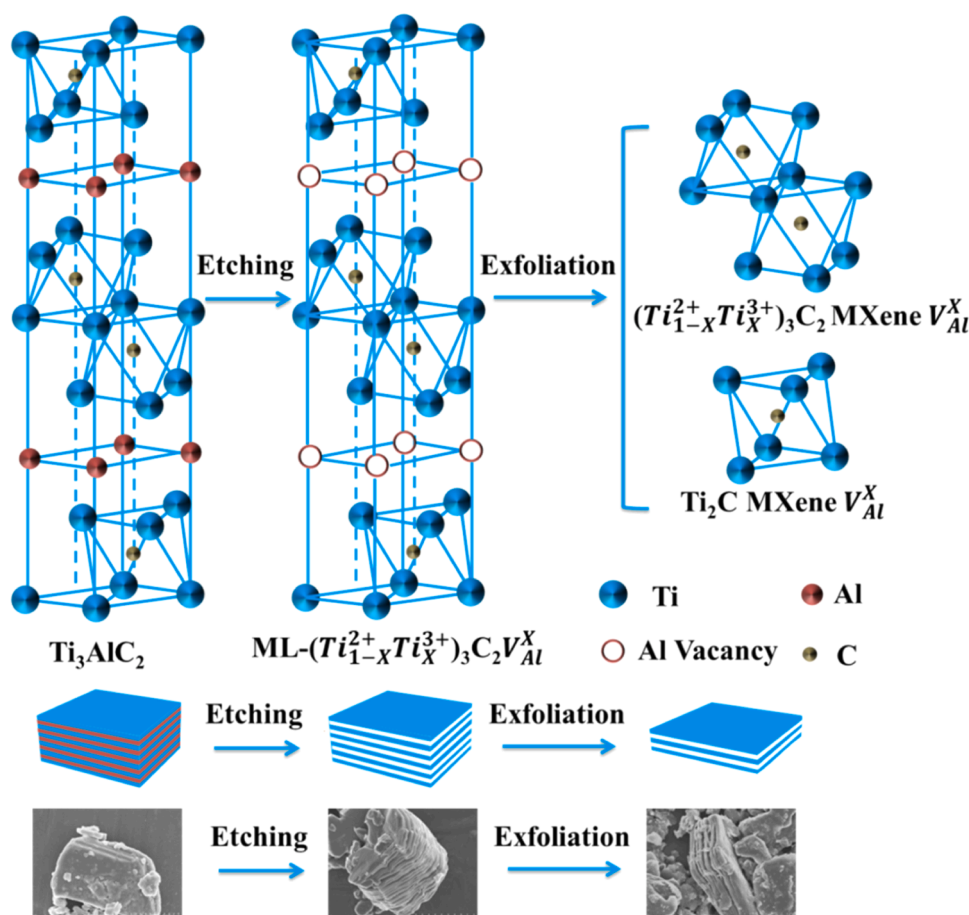

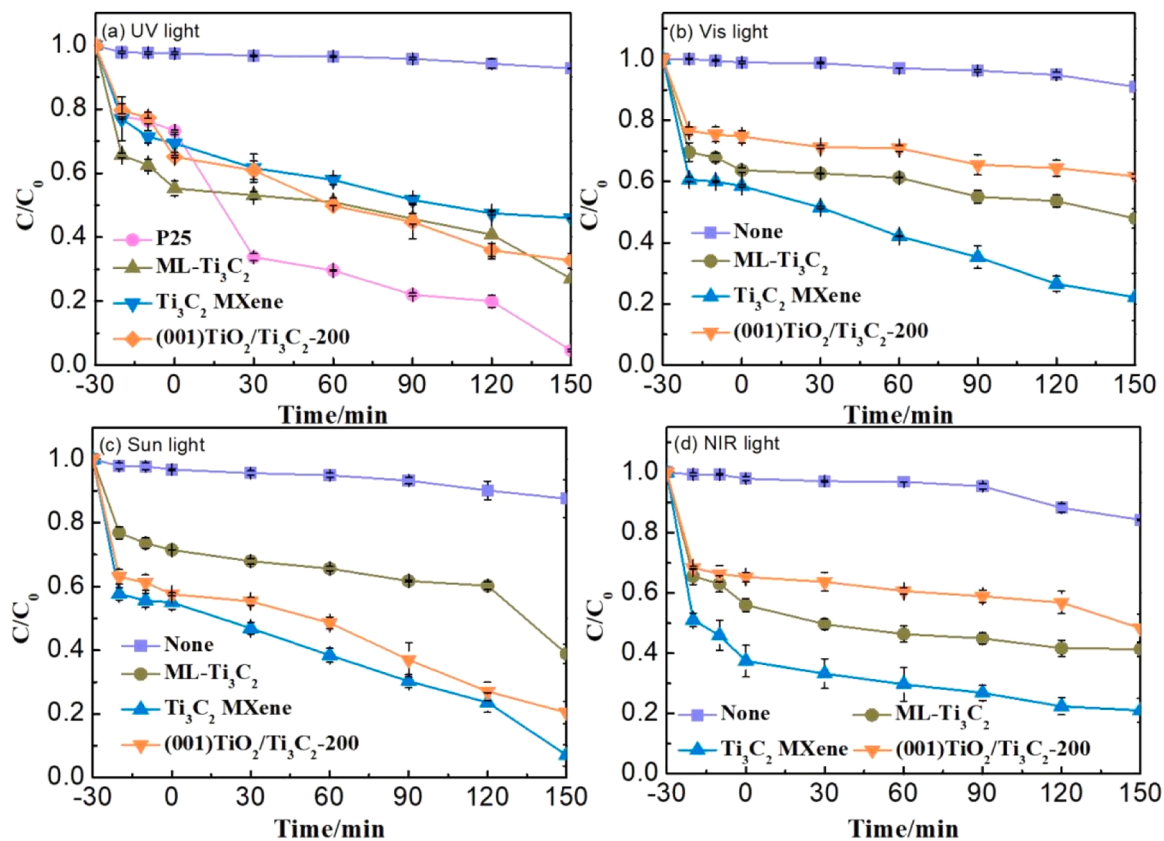**Fig. 5.** Formation process of Ti_3C_2 MXene.

Fig. 6. Degradation curves of TC by Ti_3C_2 MXene under different lights (a) UV light, (b) vis light, (c) sun light, (d) NIR light.
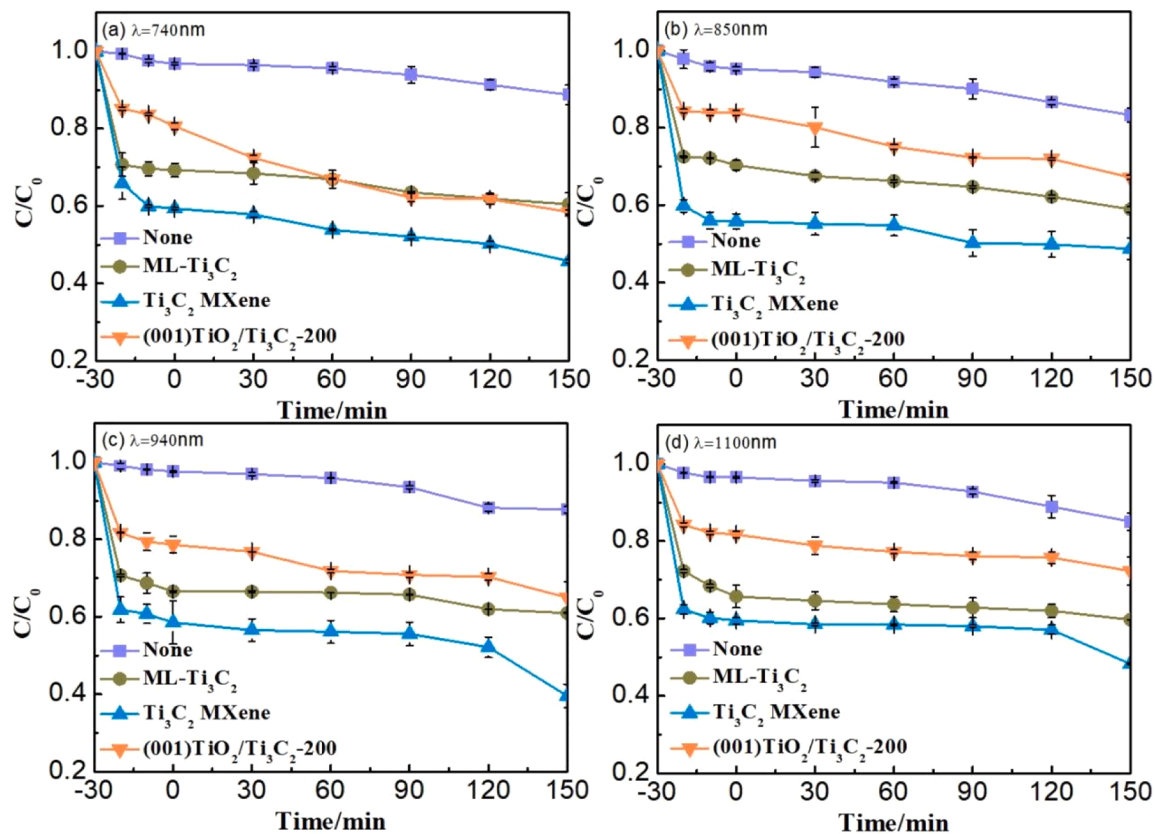

Fig. 7. Degradation curves of TC by Ti_3C_2 MXene under different monochromatic lights (a) 740 nm, (b) 850 nm, (c) 940 nm, (d) 1100 nm.

degradation rate constants (*K*) are 0.00161 min^{-1}, 0.00695 min^{-1} and 0.00127 min^{-1}, respectively (Fig. S2(b)). After 150 min of sun light illumination, the degradation rates of ML-Ti$_3$C$_2$, Ti$_3$C$_2$ MXene and (001) TiO$_2$/Ti$_3$C$_2$-200 are 61.13%, 92.92% and 79.55%, respectively (Fig. 6 (c)), and the degradation rate constants (*K*) are 0.00267 min^{-1}, 0.01007 min^{-1} and 0.00604 min^{-1}, respectively (Fig. S2(c)). After 150 min of NIR light illumination (light power=23.2 mW/cm^2), the degradation rates of ML-Ti$_3$C$_2$, Ti$_3$C$_2$ MXene and (001)TiO$_2$/Ti$_3$C$_2$-200 are 58.65%, 78.91% and 51.69%, respectively (Fig. 6(d)), and the degradation rate constants (*K*) are 0.00234 min^{-1}, 0.00394 min^{-1} and 0.00155 min^{-1}, respectively (Fig. S2(d)). These results indicate that Ti$_3$C$_2$ MXene has obvious degradation effects on TC in the full spectral range.

Fig. 7 shows the degradation curves of TC by Ti$_3$C$_2$ MXene at 740 nm, 850 nm, 940 nm and 1100 nm wavelengths (light power=61.5 mW/cm^2). After 150 min of monochromatic light irradiation, the degradation rates of ML-Ti$_3$C$_2$, Ti$_3$C$_2$ MXene and (001)TiO$_2$/Ti$_3$C$_2$-200 to TC under 740 nm monochromatic light are 39.57%, 54.23% and 41.54% respectively. The degradation rates of ML-Ti$_3$C$_2$, Ti$_3$C$_2$ MXene and (001)TiO$_2$/Ti$_3$C$_2$-200 to TC under 850 nm monochromatic light are 41.08%, 51.29% and 32.81%, respectively. The degradation rates of ML-Ti$_3$C$_2$, Ti$_3$C$_2$ MXene and (001)TiO$_2$/Ti$_3$C$_2$-200 to TC under 940 nm monochromatic light are 39.03%, 60.46% and 34.98%, respectively. The degradation rates of ML-Ti$_3$C$_2$, Ti$_3$C$_2$ MXene and (001)TiO$_2$/Ti$_3$C$_2$-200 to TC under 1100 nm monochromatic light are 40.32%, 51.76% and 27.72%, respectively. The monochromatic photodegradation experiments further prove that Ti$_3$C$_2$ MXene has good degradation properties of antibiotic TC under near-infrared light.

3.3. The photocatalytic mechanism of Ti$_3$C$_2$ MXene

Fig. 8 shows the capture of Ti$_3$C$_2$ MXene active species and EPR spectra under NIR light. P-benzoquinone (BQ), ethylenediaminetetra-acetic acid disodium (EDTA-2Na) and tert-butanol (TBA) are used as traps to ·O$_2^-$, h$^+$ and ·OH, respectively. When EDTA-2Na is added to TC solution of Ti$_3$C$_2$ MXene under NIR light for 150 min, the photocatalytic activity of EDTA-2Na is obviously inhibited and the degradation rate is only 10.03% the photocatalytic activity of EDTA-2Na is obviously inhibited and the degradation rate is only 10.03% and the degradation rate is 0.005 min^{-1}. When BQ and TBA are added, the degradation rates of TC by Ti$_3$C$_2$ MXene are 47.57% and 40.22% and the degradation rates are 0.00216 min^{-1} and 0.0015 min^{-1}, respectively, as shown in Fig. 8 and the illustrations of Fig. 8. The results show that h$^+$ is the main active substance in the degradation of Ti$_3$C$_2$ MXene under NIR light, while ·OH and ·O$_2^-$ play a secondary role in the degradation process. This is consistent with the active species capture results of Ti$_3$C$_2$ MXene for RhB degradation under NIR degradation and TC degradation under visible light (Fig.S11). In addition, in the EPR spectra of DMPO-·O$_2^-$ and DMPO-·OH, there is almost no signal under dark light. Under NIR light, four strong characteristic peaks of DMPO-·O$_2^-$ and OH radical are observed on Ti$_3$C$_2$ MXene, which indicates that the photoinduced reduction reaction between electrons and O$_2$ molecules produces a high concentration of free radicals ·O$_2^-$ (Fig. 8(b)-(c)). Moreover, the signal intensity of DMPO-·O$_2^-$ and DMPO-·OH is increased with the prolongation of NIR light, which demonstrates that ·OH radical and ·O$_2^-$ radical will be generated under NIR light. In the EPR spectrum of DMPO-h$^+$, there is a strong signal under dark light, and Ti$_3$C$_2$ MXene can be observe the signal under NIR light apparently. The signal of DMPO-h$^+$ is decreased with the prolongation of NIR light, indicating that the amount of photogenic h$^+$ is increased with the increase of light time (Fig. 8(d)). These results further suggest that h$^+$ is the main active species in Ti$_3$C$_2$ MXene degradation, while ·OH and ·O$_2^-$ play a secondary role in the degradation process.

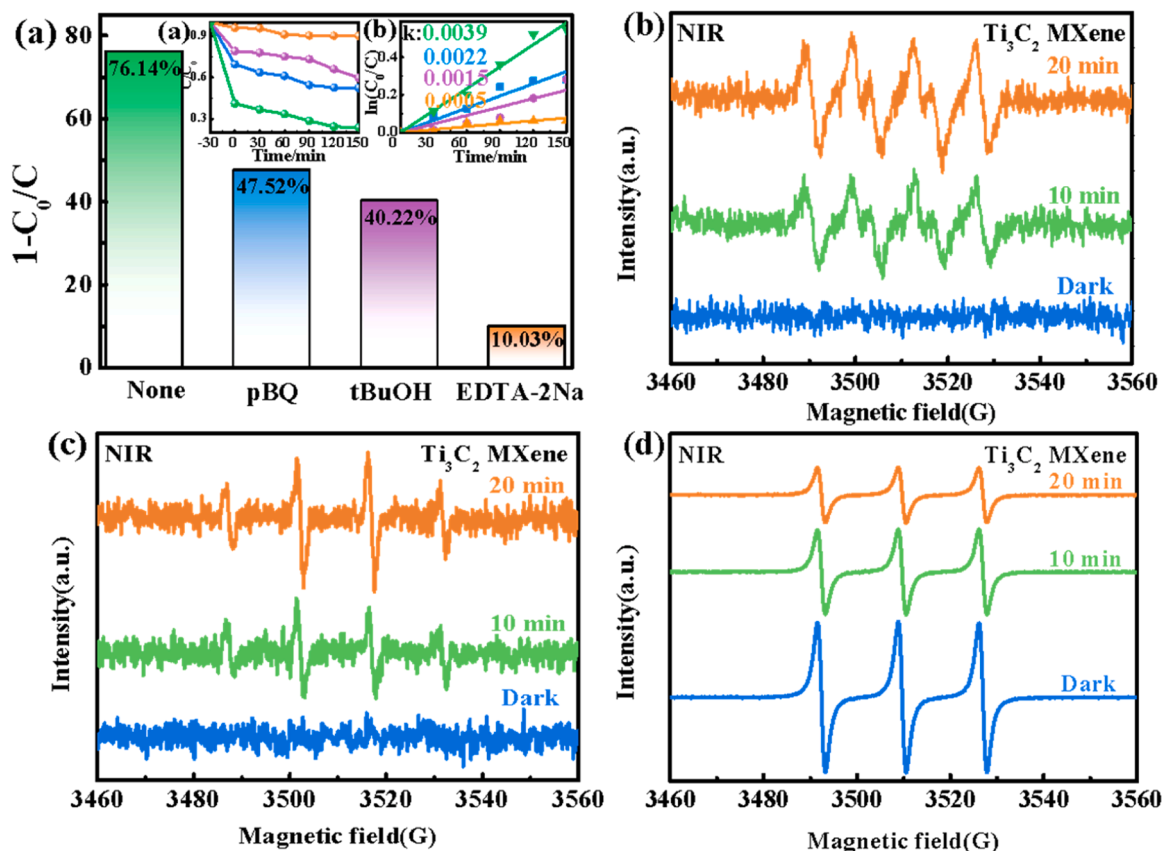The total density maps (TDOS) of different valence states of Ti in

Fig. 8. (a) Capture of active species of Ti$_3$C$_2$ MXene in NIR light, (b) EPR spectra of ·O$_2^-$, (c) ·OH, (d) h$^+$.

Ti$_3$C$_2$ MXene and the partial density maps (PDOS) of Ti 1s, Ti 2p and Ti 3d are calculated by first-principles DFT. Fig. 9(a)-(c) are the densities of Ti^{2+}, Ti^{3+} and Ti^{3+} states in the energy range of − 12–24 eV, respectively. As can be seen from the figures, DOS in S and P orbitals do not show local spikes, which indicates that the electrons in S and P orbitals are non-localized. According to the previous reports, for the transition metal Ti, the DOS of the d orbital is a large peak, which indicates that the electrons of the d orbital are relatively local [43,44]. DFT calculation results prove that Al vacancy can form the local hole in Ti$_3$C$_2$ MXene. In addition, the electromagnetic field intensities around Ti$_3$AlC$_2$ and Ti$_3$C$_2$ MXene are simulated by the finite difference time domain (FDTD) calculation. The local electric field enhancement factor is defined as | E|^2/|E$_0$|^2, where |E| and |E$_0$| represent the sizes of local electric field and the incident electric field respectively. Fig. 10(a)-(c) show that the local electric field distribution of Ti$_3$AlC$_2$ and Ti$_3$C$_2$ MXene is excited at 960 nm and Ti$_3$C$_2$ MXene is excited at 580 nm, respectively. The maximum electric field strengths (|E|^2/|E$_0$|^2) of Ti$_3$AlC$_2$ and Ti$_3$C$_2$ MXene under 960 nm excitation are 1.34 and 5.02 respectively, and the maximum electric field strength (|E|^2/|E$_0$|^2) of Ti$_3$C$_2$ MXene under 580 nm excitation is 1.46. The interfacial electric field intensity of Ti$_3$C$_2$ MXene under 960 nm excitation is obviously higher than that of Ti$_3$AlC$_2$, and the interfacial electric field intensity of Ti$_3$C$_2$ MXene under 580 nm excitation is higher than that of Ti$_3$AlC$_2$ under 960 nm excitation. FDTD calculation results show that the electric field intensity is increased after Ti$_3$AlC$_2$ is exfoliated to form Ti$_3$C$_2$ MXene. Figs. 9 and 10 jointly prove that Ti$_3$C$_2$ MXene has the local cavity state and the LSPR effect.

Combining the above experimental and theoretical calculation results, a possible photocatalytic degradation mechanism of Ti$_3$C$_2$ MXene is proposed, as shown in Fig. 11. When plasma Ti$_3$C$_2$ MXene is irradiated by a UV–visible-NIR light, the holes distributed on the surface of $(Ti^{2+}_{1-X}Ti^{3+}_X)_3C_2V^X_{Al}$ MXene and Ti$_2$CV$^X_{Al}$ MXene crystals are excited into high-energy hot holes, which directly oxidizes antibiotic TC, CIP and organic pollutants into small molecules. Under the action of the electric field strength formed by the localized hole state of Ti$_3$C$_2$ MXene, the electrons bound in the crystal of $(Ti^{2+}_{1-X}Ti^{3+}_X)_3C_2V^X_{Al}$ MXene and Ti$_2$CV$^X_{Al}$ MXene are excited and lag behind the surface of hole migration to form high-energy hot electrons, which can react with O$_2$ molecules adsorbed on the surface of TC, CIP and organic pollutants to generate ·O$_2^-$ free radicals (O$_2$ +e$^-$=·O$_2^-$). The resulting ·O$_2^-$ radical can react with H$^+$ and electrons to produce H$_2$O$_2$ (·O$_2^-$+2 H$^+$+e$^-$=H$_2$O$_2$) or directly react with two electrons and two H$^+$ to produce H$_2$O$_2$ (O$_2$ +2e$^-$+2 H$^+$=H$_2$O$_2$)·H$_2$O$_2$ molecules are further dissociated to form ·OH radical (H$_2$O$_2$ +e$^-$=·OH+OH$^-$), and induce degradation of TC, CIP, RhB and MO molecules, which is consistent with the experimental results of active species.

Fig. 12(a) shows the transient photocurrent-time curves of Ti$_3$C$_2$ MXene in vis light with a bias of 0.1 V and an interval of 20 s. ML-Ti$_3$C$_2$ produces an anode spike peak at the moment of turning on the light (1 s), and the peak photocurrent can reach 5.880 μA. After 10 s, it reaches a steady state, and the steady-state photocurrent drops to 3.160 μA. When the light is turned off, a cathodic spike peak is generated, and the peak photocurrent is − 0.429 μA, and the photocurrent recovers to 0 μA

after 10 s. Ti$_3$C$_2$ MXene also produces an anode spike peak at the moment of turning on the light, but the peak photocurrent is as high as 6.790 μA, and reaches a steady state after 10 s, with a steady-state photocurrent of 4.070 μA, and a cathodic spike peak at the moment of turning off the light, and with a photocurrent of 0.059 μA for 10 s after the photocurrent is restored to 0 μA. (001)TiO$_2$/Ti$_3$C$_2$-200 produces a weak anode spike peak at the moment of turning on the light, while the peak photocurrent is 1.040 μA, and reaches a steady state after 1 s. The steady-state photocurrent is 0.796 μA, and a cathodic spike peak is generated at the moment of turning off the light. For the peak light, the current is − 0.455 μA, and the photocurrent returns to 0 μA after 10 s. The absolute value of photocurrent response of Ti$_3$C$_2$ MXene is the strongest under visible light, and (001)TiO$_2$/Ti$_3$C$_2$-200 is weakened.

Fig. 12(b) shows the transient photocurrent-time curves of Ti$_3$C$_2$ MXene under NIR light with a bias of 0.1 V and an interval of 20 s. ML-Ti$_3$C$_2$ generates an anode spike peak at the moment of turning on the light, and the peak photocurrent is 0.017 μA. After 20 s, the photocurrent drops to − 0.111 μA. When the light is turned off, a cathodic spike peak is generated, and the peak photocurrent is − 0.237 μA. After 10 s, the photocurrent returns to 0 μA. Ti$_3$C$_2$ MXene also generates an anode spike peak at the moment of turning on the light. The peak photocurrent is − 0.191 μA, and after 20 s, the photocurrent drops to − 0.248 μA, and a cathodic spike peak is generated at the moment of turning off the light. The peak photocurrent is − 0.336 μA, and the 20 s light current returns to 0 μA. (001)TiO$_2$/Ti$_3$C$_2$-200 produces an anode spike peak at the moment of turning on the light, and the photocurrent is − 0.282 μA and reaches a steady state after 20 s. The photocurrent is − 0.341 μA, and a cathodic spike peak is generated at the moment when the light is turned off, while the photocurrent is − 0.433 μA, and the photocurrent quickly recovers to 0 μA. The absolute value of the photocurrent response of (001)TiO$_2$/Ti$_3$C$_2$-200 under near-infrared light is the strongest, and that of ML-Ti$_3$C$_2$ is weakened. This result is consistent with the EPR spectra of Ti$_3$C$_2$ MXene in Fig. 4(a).

Under vis light, ML-Ti$_3$C$_2$, Ti$_3$C$_2$ MXene and (001)TiO$_2$/Ti$_3$C$_2$ have holes distributed on the crystal surface, and the electrons bound in the crystal migrate to form photocurrent at the moment when the lamp is turned on. The number of holes distributed on the crystal surface is greater than that of the bound electrons, and the holes migrate to the surface of the cathode when the light is turned off. (001)TiO$_2$/Ti$_3$C$_2$ cannot be excited in vis light, so the absolute value of photocurrent response is weakened.

Under NIR light, the holes of Ti$_3$C$_2$ MXene and ML-Ti$_3$C$_2$ are excited into high-energy hot holes and hot electrons when the lights are turned on, and the high-energy hot holes form photocurrent. (001)TiO$_2$/Ti$_3$C$_2$ has the strongest current response absolute value, which is the LSPR of Ti$_3$C$_2$ MXene and Ti$_3$C$_2$ MXene surface plasmon effects. The resonance effect of the local magnetic field can make TiO$_2$ generate electron-hole pairs. Under the electric field of the localized hole state of Ti$_3$C$_2$ MXene, TiO$_2$ photogenerated holes are injected into Ti$_3$C$_2$ MXene, which enhances the (001)TiO$_2$/Ti$_3$C$_2$ photocurrent, and also further proves that Ti$_3$C$_2$ MXene has TE and TM waves. The surface plasmon effect can accelerate the photoexcitation of TiO$_2$ to form electron-hole pairs.
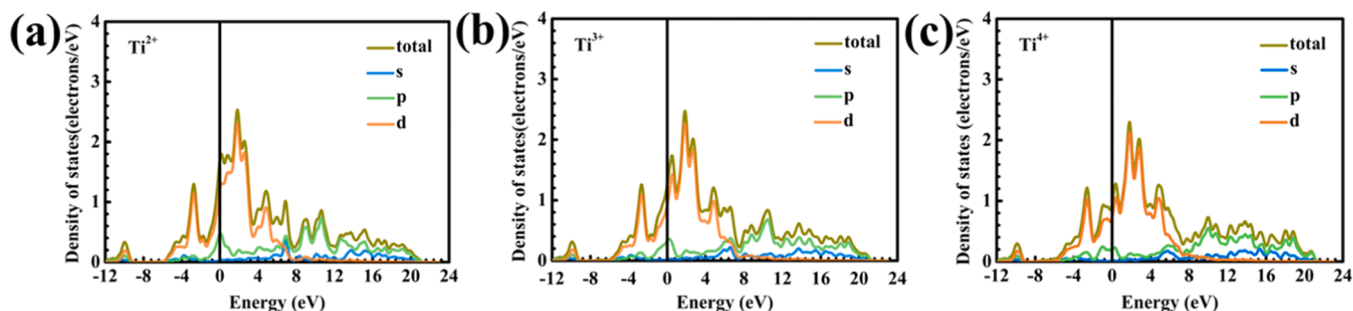

Fig. 9. Electron densities of Ti$_3$C$_2$ MXene (a) Ti^{2+}, (b) Ti^{3+}, and (c) Ti^{4+}.
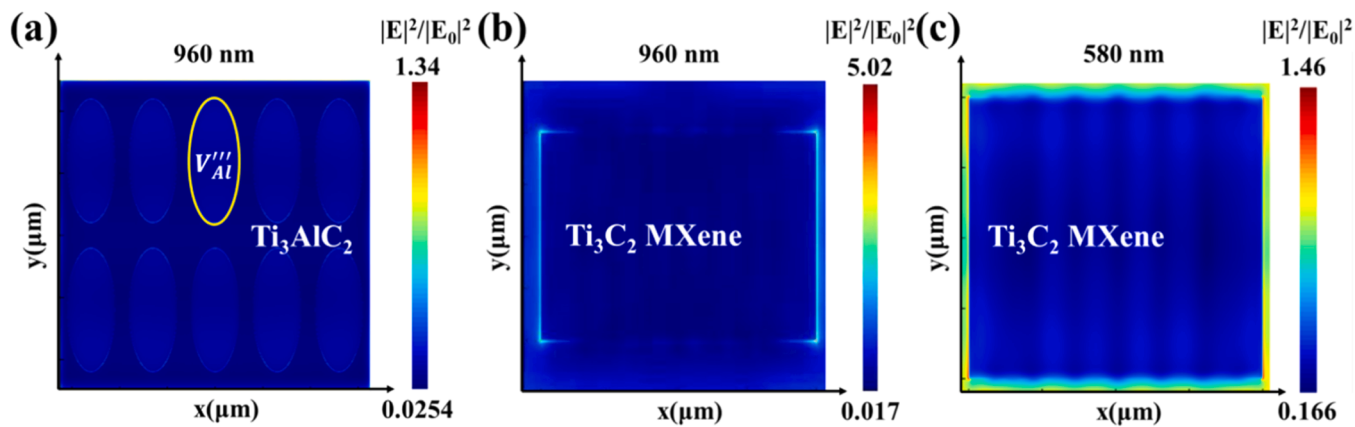
Fig. 10. (a) Ti_3AlC_2, (b)-(c) simulated electric field intensity distribution diagrams of Ti_3C_2 MXene.
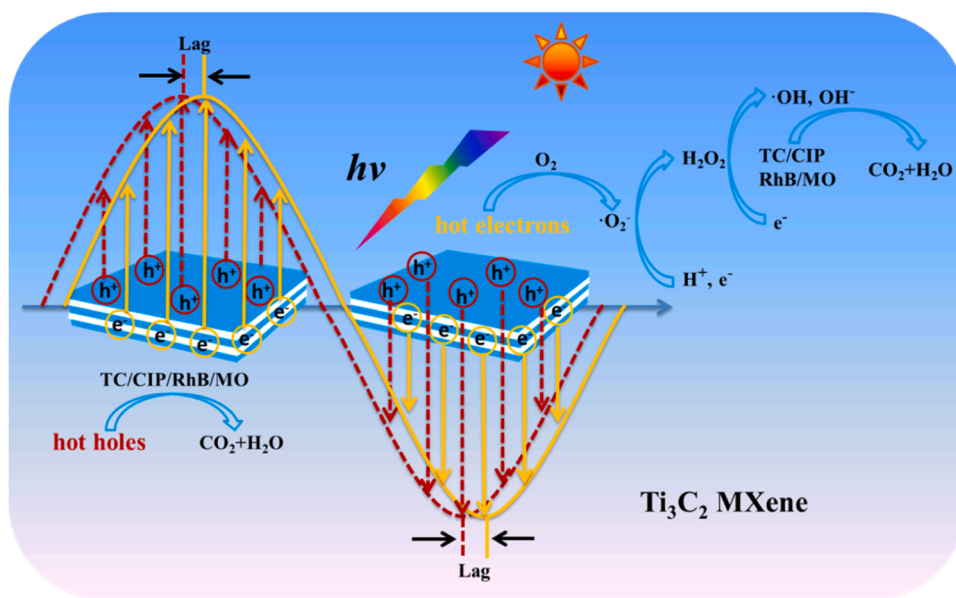

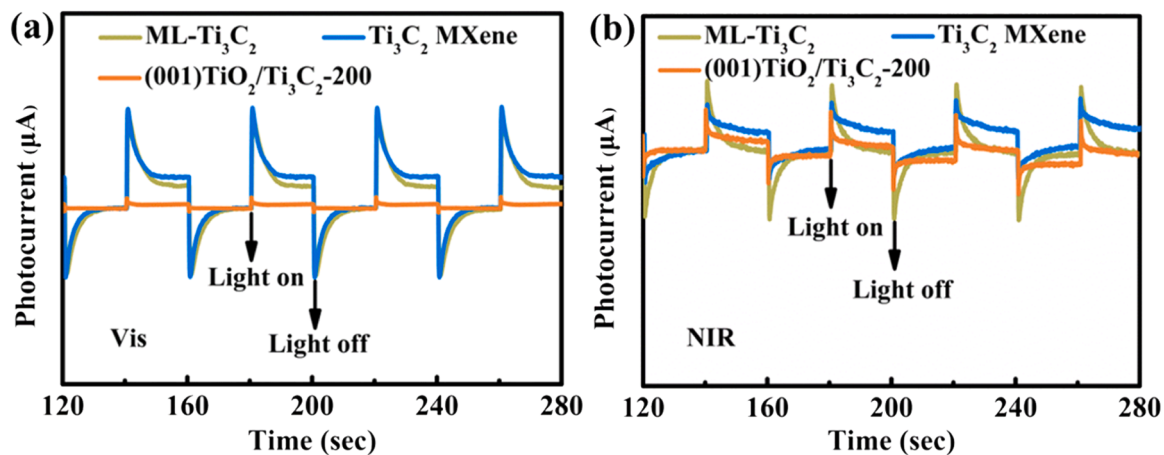**Fig. 11.** Reaction mechanism diagram of Ti_3C_2 MXene for degrading antibiotics.

Fig. 12. Current-time curves of Ti_3C_2 MXene in (a) vis and (b) near infrared light.

4. Conclusions

Ti$_3$AlC$_2$ is etched by HF to obtain the crystal of ML-$(Ti_{1-X}^{2+}Ti_X^{3+})_3C_2V_{Al}^X$(ML-Ti$_3C_2$), which is then broken and exfoliated into the crystal of Ti$_3$C$_2$ MXene with coexistence of $(Ti_{1-X}^{2+}Ti_X^{3+})_3C_2V_{Al}^X$ MXene and Ti$_2$CV$_{Al}^X$ MXene by ultrasound in water. Ti$_3$C$_2$ MXene exhibits the surface plasmon effects of transverse and longitudinal surface plasmon resonance due to the distributed holes on the surface and internal bound electrons on Ti$_3$C$_2$ MXene. High-energy hot holes on the surface of plasmonic Ti$_3$C$_2$ MXene crystals directly oxidize antibiotics and organic pollutants into small molecules under illumination. The electrons bound in the crystal are delayed by the hole excitation and then migrate to the surface to form high-energy hot electrons which react with the adsorption of O$_2$ to generate ·O$_2^-$ to induce the degradation of antibiotics and organic pollutants. After 150 min of NIR irradiation, the degradation rates of TC and CIP by Ti$_3$C$_2$ MXene are 78.91% and 99.26%, respectively. They are 1.35/1.00 and 1.53/3.11 times of ML-Ti$_3$C$_2$ and (001) TiO$_2$/Ti$_3$C$_2$. The product P10 ($m/z = 116$) is obtained through a series of hydroxylation dihydroxylation and dehydration reactions of TC, which is eventually mineralized into CO$_2$ and H$_2$O. After 120 min of near-infrared light irradiation, the degradation rates of Ti$_3$C$_2$ MXene to RhB and MO are 92.65% and 63.73%, respectively, and Ti$_3$C$_2$ MXene to DER and DR mineralization rates are 92.37% and 62.96%, respectively. The results indicate that Ti$_3$C$_2$ MXene has obvious degradation effects to antibiotics and organic dyes in the full spectral range. Our work is expected to provide a valuable reference for the design and the synthesis of the MXene full-spectral photocatalyst, and intends to expand the application of MXene-based materials in the field of photocatalysis.

CRediT authorship contribution statement

Bixin Zhang, Yong Wang, Zeqiong Wang and Guoqiang Tan conceived the idea and co-wrote the paper. Bixin Zhang, Yong Wang and Zeqiong Wang carried out the sample synthesis, characterization and photocatalytic degradation experiments. Bixin Zhang, Yong Wang, Zeqiong Wang, Guoqiang Tan, Tian Liu, Shuaijun Feng, Yizhe Tan, Wenlong Liu, Qian Yang and Ying Liu interpreted the data. Huijun Ren was mainly responsible for polishing the language. Ao Xia and Yuanting Wu provided some help during the experimental work.

Declaration of Competing Interest

The authors declare that they have no known competing financial interests or personal relationships that could have appeared to influence the work reported in this paper.

Data Availability

Data will be made available on request.

Acknowledgments

Appendix A. Supporting information

Supplementary data associated with this article can be found in the online version at doi:10.1016/j.apcatb.2023.123132.

References

[1] K.S. Novoselov, A.K. Geim, S.V. Morozov, D. Jiang, Y. Zhang, S.V. Dubonos, I. V. Grigorieva, A.A. Firsov, Electric field in atomically thin carbon films, Science. 306 (2004) 666–669.

[2] Q. Bao, K.P. Loh, Graphene photonics, plasmonics, and broadband optoelectronic devices, ACS Nano. 6 (2012) 3677–3694.

[3] Y. Wang, G. Tan, B. Li, M. Dang, L. Lv, M. Wang, D. Zhang, H. Ren, A. Xia, Enhanced NIR photocatalytic of Ag-RGO@{010}BiVO$_4$/RGO@{110} BiVO$_4$ photocatalysts induced by resonance effect of transverse electric of RGO and transverse magnetic of Ag, Appl. Surf. Sci. 489 (2019) 1–12.

[4] X. Zhang, C. Si, J. Zhou, Z. Sun, MXene and MXene-based composites: synthesis, properties and environment-related applications, Nanoscale Horiz. 5 (2020) 235–258.

[5] H. Fang, Y. Pan, M. Yin, C. Pan, Enhanced photocatalytic activity and mechanism of Ti$_3$C$_2$-OH/Bi$_2$WO$_6$:Yb^{3+}, Tm^{3+} towards degradation of RhB under visible and near infrared light irradiation, Mater. Res. Bull. 121 (2020), 110618.

[6] F. Xu, D. Zhang, Y. Liao, G. Wang, X. Shi, H. Zhang, Q. Xiang, Synthesis and photocatalytic H$_2$-production activity of plasma-treated Ti$_3$C$_2$T$_x$ MXene modified graphitic carbon nitride, J. Am. Ceram. Soc. 103 (2020) 849–858.

[7] H. Zou, B. He, P. Kuang, J. Yu, K. Fan, Metal-organic framework-derived nickel-cobalt sulfide on ultrathin mxene nanosheets for electrocatalytic oxygen evolution, ACS Appl. Mater. Interfaces. 10 (2018) 22311–22319.

[8] Q. Tang, Z. Zhou, P. Shen, Are MXenes promising anode materials for Li ion batteries? computational studies on electronic properties and Li storage capability of Ti$_3$C$_2$ and Ti$_3$C$_2$X$_2$ (X=F, OH) monolayer, J. Am. Chem. Soc. 134 (2012) 16909–16916.

[9] M. Naguib, M. Kurtoglu, V. Presser, J. Lu, J. Niu, M. Heon, L. Hultman, Y. Gogotsi, M.W. Barsoum, Two-dimensional nanocrystals produced by exfoliation of Ti$_3$AlC$_2$, Adv. Mater. 23 (2011) 4248–4253.

[10] K.M. Mayer, J.H. Hafner, Localized surface plasmon resonance sensors, Chem. Rev. 111 (2011) 3828–3857.

[11] O. Mashtalir, K.M. Cook, V.N. Mochalin, M. Crowe, M.W. Barsoum, Y. Gogotsi, Dye adsorption and decomposition on two-dimensional titanium carbide in aqueous media, J. Mater. Chem. A. 2 (2014) 14334–14338.

[12] Y. Wang, G. Tan, T. Liu, Y. Su, H. Ren, X.L. Zhang, A. Xia, L. Lv, Y. Liu, Photocatalytic properties of the g-C$_3$N$_4$/{010} facets BiVO$_4$ interface Z-Scheme photocatalysts induced by BiVO$_4$ surface heterojunction, Appl. Catal. B Environ. 234 (2018) 37–49.

[13] M. Wang, G. Tan, D. Zhang, B. Li, L. Lv, Y. Wang, H. Ren, X.L. Zhang, A. Xia, Y. Liu, Defect-mediated Z-scheme BiO$_{2-x}$/Bi$_2$O$_{2.75}$ photocatalyst for full spectrum solar-driven organic dyes degradation, Appl. Catal. B Environ. 254 (2019) 98–112.

[14] M. Wang, G. Tan, S. Feng, M. Dang, Y. Wang, B. Zhang, H. Ren, L. Lv, A. Xia, W. Liu, Y. Liu, Defects and internal electric fields synergistically optimized g-C$_3$N$_{4-x}$/BiOCl/WO$_{2.92}$ heterojunction for photocatalytic NO deep oxidation, J. Hazard. Mater. 408 (2021), 124897.

[15] Y. Gao, L. Wang, A. Zhou, Z. Li, J. Chen, H. Bala, Q. Hu, X. Cao, Hydrothermal synthesis of TiO$_2$/Ti$_3$C$_2$ nanocomposites with enhanced photocatalytic activity, Mater. Lett. 150 (2015) 62–64.

[16] Z. Miao, G. Wang, X. Zhang, X. Dong, Oxygen vacancies modified TiO$_2$/Ti$_3$C$_2$ derived from MXenes for enhanced photocatalytic degradation of organic pollutants: The crucial role of oxygen vacancy to Schottky junction, Appl. Surf. Sci. 528 (2020), 146929.

[17] Z. Li, H. Zhang, L. Wang, X. Meng, J. Shi, C. Qi, Z. Zhang, L. Feng, C. Li, 2D/2D BiOBr/Ti$_3$C$_2$ heterojunction with dual applications in both water detoxification and water splitting, J. Photochem. Photobiol. A Chem. 386 (2020), 112099.

[18] R. Li, L. Zhang, L. Shi, P. Wang, MXene Ti$_3$C$_2$: an effective 2D light-to-heat conversion material, ACS Nano. 11 (2017) 3752–3759.

[19] D. Xu, Z. Li, L. Li, J. Wang, Insights into the photothermal conversion of 2D MXene nanomaterials: synthesis, mechanism, and applications, Adv. Funct. Mater. 30 (2020) 2000712.

[20] Z. Lou, M. Fujitsuka, T. Majima, Pt-Au triangular nanoprisms with strong dipole plasmon resonance for hydrogen generation studied by single-particle spectroscopy, ACS Nano. 10 (2016) 6299–6305.

[21] Z. Lou, S. Kim, P. Zhang, X. Shi, M. Fujitsuka, T. Majima, In situ observation of single au triangular nanoprism etching to various shapes for plasmonic photocatalytic hydrogen generation, ACS Nano. 11 (2017) 968–974.

[22] D. Tian, H. Yin, H. Liu, B. Li, J. Li, Z. Lou, Plasmonic carbon nitride polymers to boost hydrogen generation, Adv. Sustain. Syst. (2022) 2200045.

[23] J. Li, Z. Lou, B. Li, Engineering plasmonic semiconductors for enhanced photocatalysis, J. Mater. Chem. A. 9 (2021) 18818–18835.

[24] Q. Zhang, J. Chen, X. Gao, H. Che, P. Wang, Y. Ao, In-depth insight into the mechanism on photocatalytic synergistic removal of antibiotics and Cr (VI): The decisive effect of antibiotic molecular structure, Appl. Catal. B Environ. 313 (2022), 121443.

[25] X. Feng, P. Wang, J. Hou, J. Qian, Y. Ao, C. Wang, Significantly enhanced visible light photocatalytic efficiency of phosphorus doped TiO$_2$ with surface oxygen vacancies for ciprofloxacin degradation: synergistic effect and intermediates analysis, J. Hazard. Mater. 351 (2018) 196–205.

[26] Q. Yang, G. Tan, B. Zhang, S. Feng, Y. Bi, Z. Wang, A. Xia, H. Ren, W. Liu, Cs$_{0.33}$WO$_3$/(t-m)-BiVO$_4$ double Z-type heterojunction photothermal synergistic enhanced full-spectrum degradation of antibiotics, Chem. Eng. J. 458 (2023), 141378.

[27] Q. Yang, G. Tan, L. Yin, W. Liu, B. Zhang, S. Feng, Y. Bi, Y. Liu, T. Liu, Z. Wang, H. Ren, A. Xia, Full-spectrum broad-spectrum degradation of antibiotics by

BiVO$_4$@BiOCl crystal plane S-type and Z-type heterojunctions, Chem. Eng. J. 467 (2023), 143450.

[28] P. Lian, Y. Dong, Z.-S. Wu, S. Zheng, X. Wang, W. Sen, C. Sun, J. Qin, X. Shi, X. Bao, Alkalized Ti$_3$C$_2$ MXene nanoribbons with expanded interlayer spacing for high-capacity sodium and potassium ion batteries, Nano Energy. 40 (2017) 1–8.

[29] B. Fan, S. Shang, B. Dai, B. Zhao, N. Li, M. Li, L. Zhang, R. Zhang, F. Marken, 2D-layered Ti$_3$C$_2$/TiO$_2$ hybrids derived from Ti$_3$C$_2$ MXenes for enhanced electromagnetic wave absorption, Ceram. Int. 46 (2020) 17085–17092.

[30] M. Hu, Z. Li, T. Hu, S. Zhu, C. Zhang, X. Wang, High-capacitance mechanism for Ti$_3$C$_2$T$_x$ MXene by in situ electrochemical raman spectroscopy investigation, ACS Nano. 10 (2016) 11344–11350.

[31] Y. Wang, G. Tan, B. Li, M. Dang, L. Lv, M. Wang, D. Zhang, H. Ren, A. Xia, Enhanced NIR photocatalytic of Ag-RGO@{010}BiVO$_4$/RGO@{110} BiVO$_4$ photocatalysts induced by resonance effect of transverse electric of RGO and transverse magnetic of Ag, Appl. Surf. Sci. 489 (2019) 1–12.

[32] H. Huang, Y. Song, N. Li, D. Chen, Q. Xu, H. Li, J. He, J. Lu, One-step in-situ preparation of N-doped TiO$_2$@C derived from Ti$_3$C$_2$ MXene for enhanced visible-light driven photodegradation, Appl. Catal. B Environ. 251 (2019) 154–161.

[33] W. Jiang, M. Zhang, J. Wang, Y. Liu, Y. Zhu, Dramatic visible activity in phenol degradation of TCNQ at TiO$_2$ photocatalyst with core-shell structure, Appl. Catal. B Environ. 160 161 (2014) 44–50.

[34] S. Huang, V.N. Mochalin, Hydrolysis of 2D transition-metal carbides (MXenes) in colloidal solutions, Inorg. Chem. 58 (2019) 1958–1966.

[35] X. Li, G. Fan, C. Zeng, Synthesis of ruthenium nanoparticles deposited on graphene-like transition metal carbide as an effective catalyst for the hydrolysis of sodium borohydride, Int. J. Hydrog. Energy. 39 (2014) 14927–14934.

[36] Yan Zhuang, Yunfei Liu, Xianfeng Meng, Fabrication of TiO$_2$ nanofibers/MXene Ti$_3$C$_2$ nanocomposites for photocatalytic H$_2$ evolution by electrostatic self-assembly, Appl. Surf. Sci. 496 (2019), 143647.

[37] J. Liu, X. Kong, Y. Li, S. Zhu, Y. Liang, Z. Li, S. Wu, C. Chang, Z. Cui, X. Yang, In situ synthesis of exfoliation TiO$_2$@C hybrids with enhanced photocatalytic hydrogen evolution activity, Appl. Surf. Sci. 530 (2020), 147283.

[38] S. Huang, V.N. Mochalin, Hydrolysis of 2D transition-metal carbides (MXenes) in colloidal solutions, Inorg. Chem. 58 (2019) 1958–1966.

[39] C. Peng, X. Yang, Y. Li, H. Yu, H. Wang, F. Peng, Hybrids of two-dimensional Ti$_3$C$_2$ and TiO$_2$ Exposing {001} facets toward enhanced photocatalytic activity, ACS Appl. Mater. Interfaces. 8 (2016) 6051–6060.

[40] X. Liu, G. Zhu, X. Wang, X. Yuan, T. Lin, F. Huang, Progress in black titania: a new material for advanced photocatalysis, Adv. Energy Mater. 6 (2016) 1–29.

[41] X. He, J. Fu, X. Fu, Y. Luo, R. Cheng, Analysis of mid-infrared graphene surface plasmons, Opt. Commun. 332 (2014) 149–153.

[42] S.A. Mikhailov, K. Ziegler, New electromagnetic mode in graphene, Phys. Rev. Lett. 99 (2007) 1–4.

[43] Q. Li, T. Liu, X. Xu, R. Guo, X. Jiao, X. Wang, Y. Lu, Study of cation vacancies with localized hole states in MgAl$_2$O$_4$ crystals, J. Phys. Chem. Solids. 145 (2020), 109542.

[44] M. Wang, G. Tan, B. Zhang, Y. Wang, Y. Bi, Q. Yang, Y. Liu, T. Liu, Z. Wang, H. Ren, L. Lv, A. Xia, L. Yin, Q. Yuan, W. Liu, Y. Liu, Synergistic integration of energy storage catalysis: a multifunctional catalytic material for round-the-clock environmental cleaning, Appl. Catal. B Environ. 321 (2023), 122052.